



# Numerical and experimental study on high-speed nailing process for aluminum/steel structures induced by electromagnetic impact

Junjia Cui<sup>1</sup> · Bingkun Li<sup>1</sup> · Hao Jiang<sup>1</sup> · Guangyao Li<sup>1</sup>

Received: 17 February 2020 / Revised: 16 April 2020 / Accepted: 4 May 2020 / Published online: 15 May 2020  
© Wrocław University of Science and Technology 2020

## Abstract

The innovation of traditional machinery manufacturing and the promotion of advanced manufacturing technology are becoming the booster for the sustainable development of automobile industry. This paper aims to propose a promising manufacturing technology driven by electromagnetic impact, which is called as electromagnetic high-speed nailing. In this paper, the connection mechanism and joint performance (e.g., microtopography and mechanical properties) of the aluminum alloy 5052 (Al)/high-strength steel DP590 (HSS) structure were studied using simulation and experiment methods. A two-dimensional axisymmetric model based on mechanical–thermal finite element analysis was proposed to explore the formation process of the joints. Microscopic observations and effective plastic strain field analysis showed that excessive deformation of the Al sheet caused serious damage to the HSS sheet, thereby making the joint more susceptible to failure. Through mechanical properties tests, it was found that the mechanical properties of the joints with different discharge energies varies. Specifically, the joints at the discharge energy of 5.3 kJ had the highest maximum shear load. While the joints at the discharge energy of 5.1 kJ showed higher push-out strength because of the better wrapping and higher interlocking degree.

**Keywords** High-speed nailing · Electromagnetic impact · Advanced manufacturing · Al/HSS joint · Mechanical properties

## 1 Introduction

The automotive industry faces the challenge of reducing carbon dioxide emissions due to environmental policies and increasing of pressure on fuel supply [1]. Replacing the original materials with new lightweight materials is an effective way to reduce vehicle weight and save energy. Therefore, the main urgent tasks are to employ the lightweight materials in automobile production [2].

For dissimilar lightweight materials, the demand for advanced connection technology becomes increasingly urgent. The existing connection technologies mainly include riveting [3], bonding [4] and bolting [5]. However, the adhesives of bonding tend to age, leading to lower reliability of the connection. Furthermore, there is often looseness in the bolting joint, which reduces the connection quality [6]. As a common and straightforward process, riveting technology

is very suitable for joining dissimilar materials [7], especially for the connection between carbon fiber and metal materials [8]. However, the conventional riveting process is prone to produce defects such as cracking of the driven head, uneven interferences and poor sealing [9]. Apart from that, the crucial limitation of the traditional riveting in automotive industry is its limited ability to automate (pre-punching, rivet positioning, etc.), which is extremely important on the production line. As one of the most efficient manufacturing techniques, electromagnetic riveting (EMR) has the advantages of high-speed impact, small impact damage, deformation stability, and large loading force, thereby ensuring a uniform interference-fit value [10].

Many studies have verified above advantages. For example, as reported by Repetto et al. [11], a finite element model to simulate the EMR process was proposed. The results demonstrated that EMR achieved a high-speed loading in a short time. Cui et al. [12] recently developed a high precision electromagnetic–mechanical–thermal coupling FE model. They found that the riveting speed at the discharge energy of 5 kJ was about 4.8 m/s, and the results were verified by experimental measurements. Huffer [13] designed a low-voltage handheld electromagnetic riveting machine with a maximum

✉ Guangyao Li  
gyli@hnu.edu.cn

<sup>1</sup> State Key Laboratory of Advanced Design and Manufacturing for Vehicle Body, Hunan University, Changsha 410082, China

impact speed of 10 m/s. In addition, Li et al. [14] further proved that by experimental methods, the fatigue performance of EMR joints was about 1–3 times higher than that of conventional pressure riveted joints. Based on the above advantages, Liang et al. [15] combined EMR technology with regular self-piercing riveting (SPR) technology, and proposed electromagnetic self-piercing riveting (E-SPR). They have demonstrated that the high strain rate in the E-SPR process had a higher strengthening effect on the rivet leg and a higher maximum shear strength comparing with the regular pressure self-piercing riveted (P-SPR) joints.

However, regular riveting is required on both sides, which makes riveting difficult under closed conditions or space-frame design. In this case, it is particularly essential to rivet from only one side. Flow-drilling screws (FDS) is a process of mechanical joining in situations with one-sided access [16]. Sønstabø et al. [17] studied the cross-tests of the FDS connection in three load directions as well as single lap and peel tests. Nagel et al. [18] carried out the push-out test on various screw joints to quantitatively evaluate the quality of the thread. Apart from this, friction stir blind riveting (FSBR) also eliminated the need for pre-drilling to insert rivets as reported by Gao et al. [19]. In contrast, the above two processes lead to longer riveting cycles and higher equipment costs.

The need for special applications, high efficiency and greater flexibility led to the development of new mechanical connection technologies. Meschut et al. [20] recently proposed a promising high-speed joining process, which had the advantages of single-sided entry, short joint period and no pre-punching. Furthermore, as reported by Goldspiegel et al. [21], high-speed nailing (HSN) could expand the perforation ability of materials, thereby expanding the range of material connections. However, the power source of current HSN process was based entirely on pneumatic pistons. In the riveting process, when it was expected to achieve high-speed conditions, the higher air pressure was required. In this case, it was easy to cause rivet force instability and joint defects. While the electromagnetic drive can not only reduce the cost of industrial equipment, but

also can be stably controlled to achieve high-speed impact. Regarding the existing literature, the HSN process induced by electromagnetic impact has not been reported.

This paper proposes a new high-speed nailing process driven by electromagnetic impact, which combined the unique advantages of EMR and HSN. Firstly, technological experiments were carried out on aluminum/steel structures with different discharge parameters. Meanwhile, the mechanism of joint formation during high-speed loading was studied by numerical simulation. Microscopic and mechanical tests were then performed to assess the quality of the joints. Finally, the failure modes of the joints were analyzed.

## 2 Materials and methods

### 2.1 Specimen preparation

In this study, 5052 Al sheets and DP590 HSS sheets were riveted using standard tacks (FK 16-8-3). The rivet material was 45B2 steel manufactured by Böllhoff. All Al sheets and HSS sheets were cut along the rolling direction. The chemical composition and mechanical properties of the sheets and rivets are listed in Table 1.

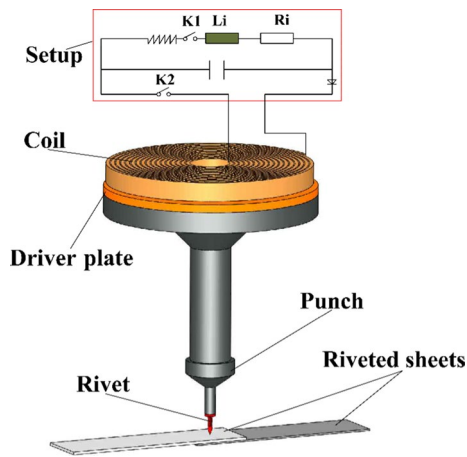
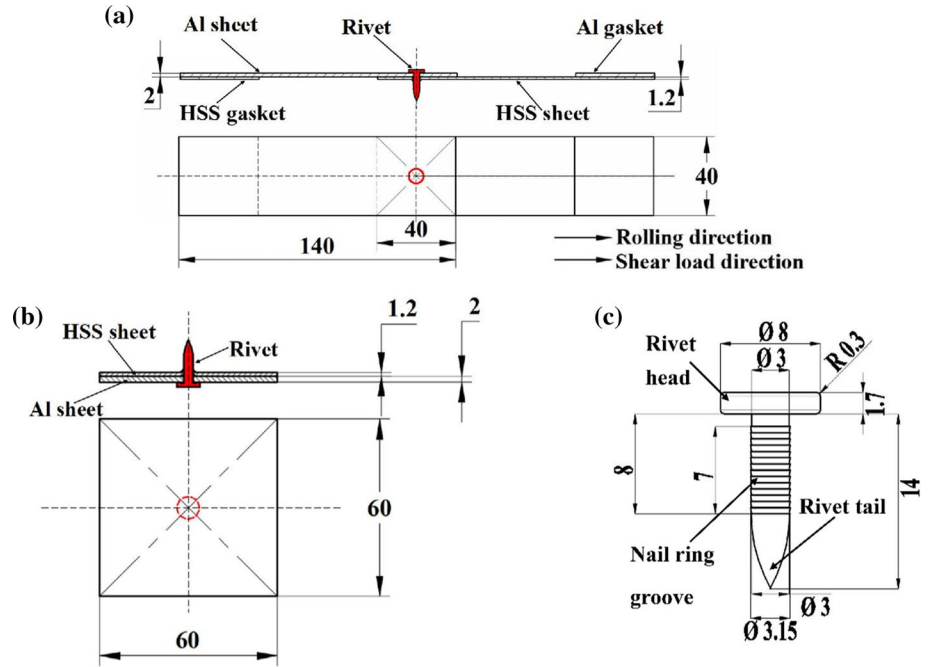
The riveted joints used for shear tests were lapped, and Fig. 1a shows the geometry of the single lap joint. The dimensions of Al and HSS sheets were  $140 \times 40 \times 2$  mm and  $140 \times 40 \times 1.2$  mm, respectively. The overlapping area was 40 mm in length. In order to prevent the specimens from bending during shear tests, all specimens were fitted with the metal gaskets of the same thickness as the sheets.

Figure 1b shows the geometry of the connector used for push-out tests. The dimensions of the Al and HSS sheets were  $60 \times 60 \times 2$  mm and  $60 \times 60 \times 1.2$  mm, respectively. The two metal sheets were overlapped entirely and then a punch was employed to push out the rivet. Figure 1c depicts the geometry dimensions of rivets.

**Table 1** Mechanical properties and chemical compositions of sheets and rivets

Properties	5052 Al sheets	DP590 HSS sheets	45B2 steel rivets
Density ( $\text{kg/m}^3$ )	2680	7812	7850
Yield strength (MPa)	148	486	$\geq 1050$
Tensile strength (MPa)	212	702	$\geq 1295$
Elasticity modulus (GPa)	70	200	200
Poisson's ratio	0.33	0.3	0.3
Chemical compositions (wt%)	Si=0.14, Fe=0.36, Cu=0.01, Mn=0.05, Mg=2.48, Cr=0.17, Al=balance	C=0.095, Si=0.16, Mn=1.9, Mo=0.09, S=0.004, Fe=balance	C=0.14–0.19, Si=0.15–0.3, Mn=0.3–0.5, S $\leq$ 0.035, Ni $\geq$ 1.4

**Fig. 1** Geometry dimensions on the riveted specimens and rivets (dimensions in mm): **a** the specimen for shear tests, **b** the specimen for push-out tests, **c** the rivets

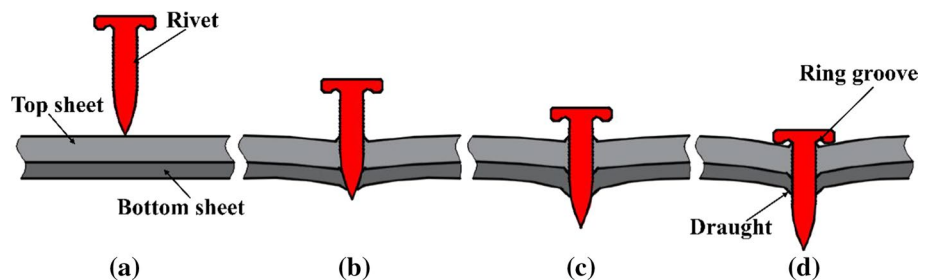


**Fig. 2** Schematic diagram of the E-HSN process

**2.2 Riveting methods**

Figure 2 shows the schematic diagram of the E-HSN process. The electromagnetic setup is to provide impact energy.

**Fig. 3** Different stages of the E-HSN process: **a** positioning, **b** penetrating sheets, **c** forming of the draught, **d** final bracing



Firstly, turn on k1 and the electromagnetic setup begins to reserve energy. After the charging process is complete, k2 is switched and the stored electrical energies are released through the discharge coil. The alternating pulse current having high amplitude passes through the coil and generates a strong electromagnetic field around it, which will further result in eddy currents in the drive plate (copper). The eddy currents will then induce an electromagnetic field. Since the direction of the electromagnetic field from the coil is opposite to that induced by the drive plate, these two magnetic fields generate a strong repulsive force and quickly drive the punch toward the rivet [22]. Under the impact of the punch, the rivet penetrates the sheets at a high speed and forms a firm connection with the sheets.

Specifically, E-HSN process is a one-step process consisting of four stages [23], as shown in Fig. 3: (a) positioning, (b) penetrating sheets, (c) forming of the draught and (d) final bracing. During high-speed impact, the plasticity and frictional work are converted into heat, causing a sudden rise in the temperature of the joint zone. High strain rates ( $> 10,000 \text{ s}^{-1}$ ) and temperatures up to  $800 \text{ }^\circ\text{C}$  can occur

around the rivet [20]. Due to the local instantaneous temperature rise, the fluidity of the material is improved [21]. The ring grooves of the rivet head and nail shank are finally filled with the sheet material to form into a shape for connection.

E-HSN experiments were performed with a PS 48-16 magnetic pulse generator (manufactured by PST Corporation, as shown in Fig. 4a) and the riveting tooling. The maximum capacitance of the PST magnetic pulse generator is 408  $\mu$ F and the maximum discharge energy is 48 kJ. By referring to the selection conditions of discharge energies by Jiang et al. [24] and carrying out some exploratory experiments, the energy used in the experiments was determined to be 4.9 kJ, 5.1 kJ, 5.3 kJ, and 5.5 kJ, respectively. As shown in Fig. 4b, the high-speed camera was used to measure the speed of the punch during high-speed impact.

### 2.3 Cross-section observation and mechanical properties test methods

In order to observe the cross-section of joints, the specimens were firstly cut longitudinally along the rivet shaft using the AbrasiMet 250 wheel cutter from Buehler. After that, the cross-section of the riveted specimens made by the SimpliMet XPS1 mounting press machine, and then polished with EcoMet 250 grinding and polishing machine. Finally, the Olympus DSX500 optical microscope was used to observe the cross-section appearance of joints. The shear tests and push-out tests were carried out by an Instron 5985 universal tester with a quasi-static speed of 2 mm/min. Figure 5 depicts the equipment and diagrams of mechanical tests.

## 3 Numerical simulation model

### 3.1 Mechanical–thermal coupled field model

In this study, an axisymmetric model based on mechanical–thermal finite element analysis (FEA) was established

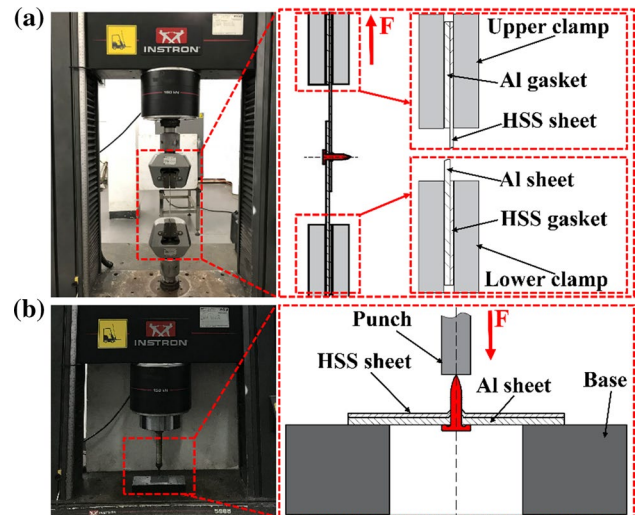


Fig. 5 Equipment and diagrams of the riveted joints for the mechanical tests: a shear tests, b push-out tests

using Simufact.Forming finite element software (MSC.Software). The finite element model is shown in Fig. 6. In order to handle the large deformation of mesh elements, automatic mesh refinement technique was used. The remeshing technique implemented was the advancing front quad method for the elements of substrate material sheets and the quadtree method for the elements of the rivet. This created the finer mesh on the boundary. The element type used for numerical simulation was a four-node isoparametric solid element. The feature of this element type was that four nodes were placed at the corners of a quadrilateral [25]. For regions with large deformation, the deformed grids were inspected according to the remeshing criterion. If the conditions were not met, the mesh repartition function would be started to map the calculation results from the previous grid to the new grid. The mesh size of the places with small deformation remained the same, so as to reduce the calculation time. After continuous debugging and improvement, the mesh sizes using for sheets and the rivet were  $0.06 \times 0.06$  mm. The number of elements

Fig. 4 The diagram of the PST magnetic pulse generator, E-HSN tooling and high-speed camera: a PST magnetic pulse generator, b the E-HSN tooling and high-speed camera



**Fig. 6** The FEM model for mechanical–thermal coupled analysis

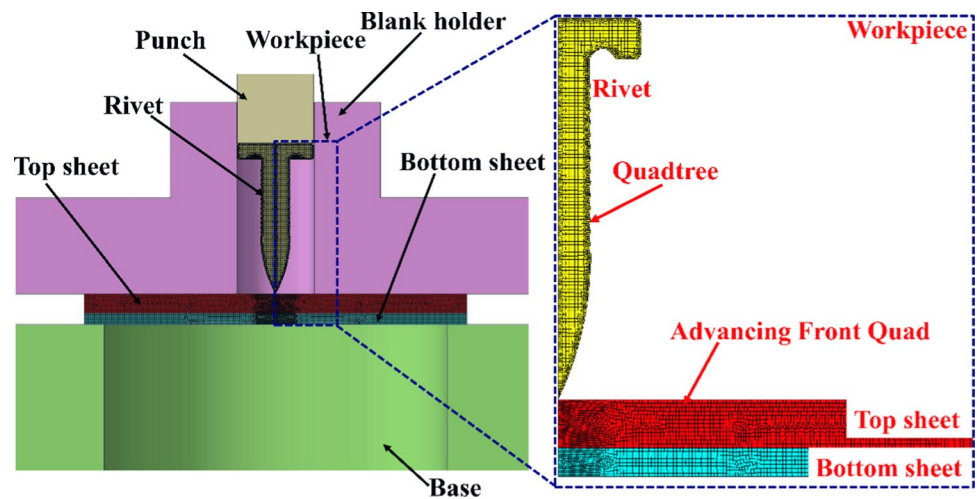
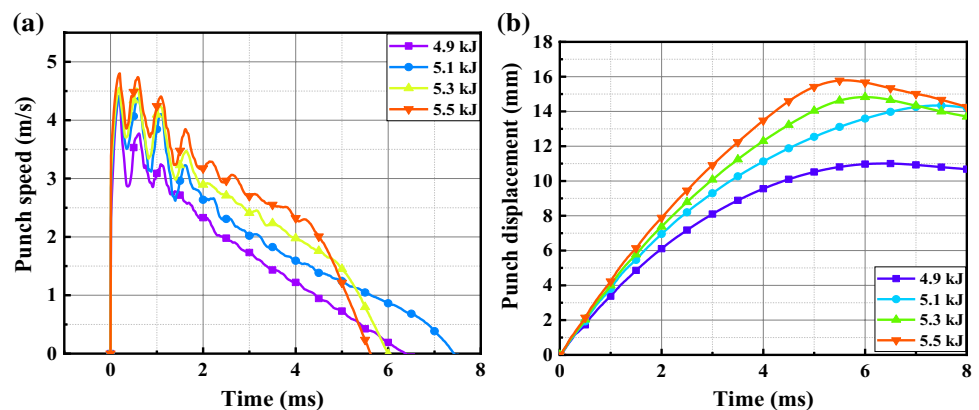


**Fig. 7** The E-HSN process punch speed–time and punch displacement–time curves: **a** punch speed–time curves, **b** punch displacement–time curves



were 11,654 for the top sheet, 7409 for the bottom sheet and 9852 for the rivet.

The riveting process included the punch down and the workpiece deformation. Figure 7 depicts punch speed–time and punch displacement–time curves obtained from the E-HSN process experiments. It could be seen that the riveting speed increased rapidly and reached the maximum value (about 5 m/s). The whole riveting process was completed within 8 ms. This further proved that E-HSN process had a higher impact velocity. The data of the punch displacement and speed were used as loading conditions for the punch. The clamping force applied by the blank holder was modeled by a compression spring with an initial force of 2.5 kN. The base and the blank holder were fixed members.

Table 2 shows the definition of the simulation parameters required for the model. Furthermore, in order to allow the splitting of the sheets during rivet insertion, geometric failure criteria were applied. The method was based on erosion techniques which allowed the elements to be deleted when a user-defined thickness value was reached. In this simulation, the minimum thickness was set to 0.03 mm, which represented that the segmentation distance was 0.03 mm.

**Table 2** The definition of the simulation parameters

Conditions	Coulomb friction	Interfacial friction	Initial temperature (°C)	Heat transfer coefficient (W/(m <sup>3</sup> K))
Parameters	0.1	0.2	20	50

Among them, since there was no large deformation and fracture during the deformation of the rivet, it was not necessary to define the fracture criterion. The type of contact between the models was face-to-face contact. In order to analyze the stress and strain distribution of joints after riveting, three conditions were defined: workpiece deformation, punch release and fixed members release.

### 3.2 Constitutive relationship of the substrate materials

During the E-HSN process, highly localized plastic deformation occurred around the rivet penetration zone, which caused some mechanical energy converting into heat. All

materials exhibited the strain rate hardening and thermal softening with the increase in loading speed and temperature as reported by Johnson and Cook [26]. Therefore, it was necessary to study the thermal softening and strain hardening in order to characterize the mechanical properties of the material. The Arrhenius hyperbolic sinusoidal constitutive equation was used to establish the constitutive relation of the metal materials studied in this paper. Its expression was:

$$\dot{\epsilon} = A[\sinh(\alpha\sigma)]^n \exp\left(-\frac{Q}{RT}\right) \quad (1)$$

where  $\dot{\epsilon}$  is the strain rate,  $\alpha$  is the stress level parameter ( $\text{MPa}^{-1}$ ),  $\sigma$  is the flow stress ( $\text{MPa}$ ),  $A$  is the structural factor ( $\text{s}^{-1}$ ),  $n$  is the stress index,  $R$  is the gas constant,  $T$  is the deformation temperature, and  $Q$  is the deformation activation energy. The relationship between strain rate and temperature was obtained by the study of Zener et al. [27], which could be represented by a parameter  $Z$ :

$$Z = \dot{\epsilon} \exp\left(\frac{Q}{RT}\right) \quad (2)$$

where  $Z$  is the Zener–Hollomon parameter which is the temperature compensated deformation rate factor. The deformation activation energy  $Q$  reflects the difficulty of thermal deformation, which is also an important mechanical property parameter of the material during the thermal deformation process. Its value is usually equal to the activation enthalpy  $\Delta H$ . The relationship between  $Z$  and  $\sigma$  is:

$$Z = A[\sinh(\alpha\sigma)]^n. \quad (3)$$

Thus, the Arrhenius hyperbolic sinusoidal constitutive equation could be expressed as a function of the Zener–Hollomon parameter  $Z$  value.

$$\sigma = \frac{1}{\alpha} \ln \left[ \left(\frac{Z}{A}\right)^{\frac{1}{n}} + \left[\left(\frac{Z}{A}\right)^{\frac{2}{n}} + 1\right]^{\frac{1}{2}} \right] \quad (4)$$

The constitutive equation parameter values of the metal materials used in this study (listed in Table 3) were taken from the experimental procedures of Zheng et al. [28] and Qiu et al. [29]. In addition, the material properties in Table 1 were used in this simulation.

### 3.3 Verification of the finite element model

The joint section has three significant structural parameters which had the direct influence on the mechanical properties of the E-HSN joints. As shown in Fig. 8, the bending distance  $B$  represented the distance from the lower part of the rivet head to the top sheet, which indirectly assessed the degree of bending for the sheets. The gap size  $G$  represented

**Table 3** Parameter values for the model of 5052 Al and DP590 HSS

Material	$A$ ( $\text{s}^{-1}$ )	$\alpha$ ( $\text{MPa}^{-1}$ )	$n$	$Q$ ( $\text{kJ/mol}$ )
5052 Al	$12.68 \times 10^{11}$	0.023	5.21	182.25
DP590 HSS	$2.126 \times 10^{17}$	0.0153	3.194	508.29

the remaining gap which based on the outside of the rivet head between the top and bottom sheet. The wrapping distance  $W$  represented the distance of the bottom sheet from the nail shank, which indicated the wrapping effect of the bottom sheet after riveting. In this study, these above structural parameters were used to verify the simulation results.

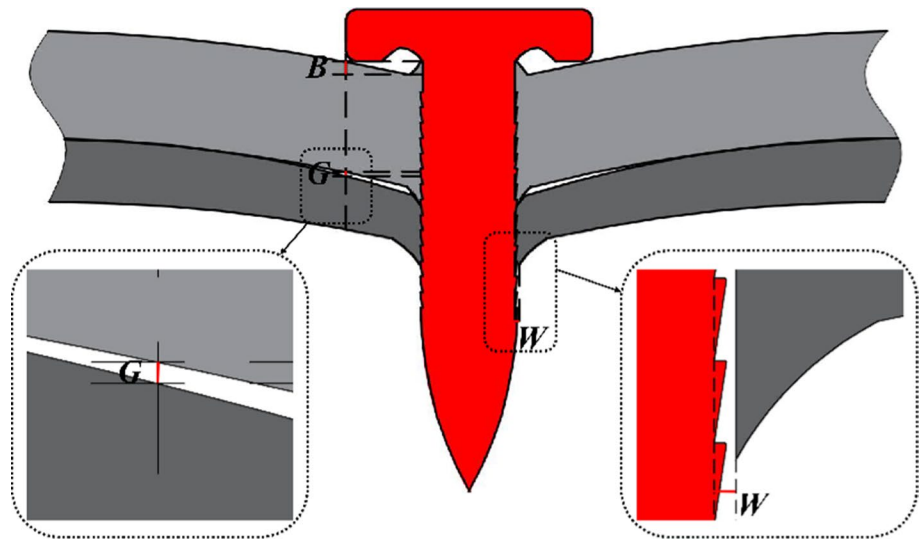
Figure 9a shows a comparison of cross-sectional geometry between experimental and numerical simulations. Good consistency could be obtained in the global cross-section comparison presented in Fig. 9a. Figure 9b shows a comparison of measured parameters. It could be seen that the compared results of the three parameters were all similar. Only the parameter  $G$  had relatively large error (18%). The average experimental parameter  $B$  was 0.6 mm, while the value predicted from numerical analysis was 0.7 mm. The predicted value of parameter  $B$  was 14% higher than that of the experimental value. Besides, it was worth mentioning that the average of experimental parameter  $W$  was 0.09 mm while the predicted value was the same. In general, the errors of these structural parameters were within 20%. So it verified that the mechanical–thermal coupled field model in this study was relatively accurate.

## 4 Results and discussion

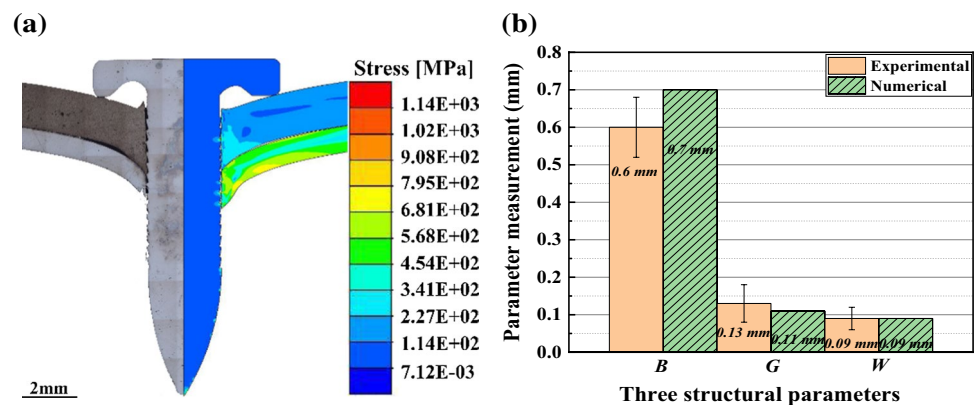
### 4.1 Connection mechanism analysis

Figure 10 presents the formation process of the joint. In this study, discharge energy of 5.1 kJ was used as an example to analyze the whole formation process. The simulation of the formation process was divided into four stages for analysis. In each stage, 10 measured points located inside the sheets failure area were selected, as shown in Fig. 10a. Further, Fig. 10b shows average effective stress evolution undergone by measured points. Before the rivet penetrated into sheets, the rivet position was determined. The blank holder was positioned on the sheets to be joined with a defined force and held them in place. When the ogival tip of the rivet penetrated the top sheet and displaced the material in the radial direction, the material in contact with the rivet flowed along the tip of nail, which counter to the joining direction. The bottom sheet was in a compression stress state until fracture of the top sheet occurred. In this stage, the average effective stress increased gradually and reached the maximum (zone 1). As the rivet continued to penetrate the bottom sheet, the

**Fig. 8** Cross-sectional geometry of the E-HSN joint showing key geometric features used to define the feature of the joint



**Fig. 9** Deformation comparisons between experimental and numerical results: **a** the comparison of cross-sectional geometry, **b** the comparison of measured parameters



material around the tail of rivet flowed in the direction of the rivet stroke. The tip of the rivet penetrated the sheets in their entirety, so that the rivet shank could achieve both a force and a form fit with the hole it had made. It could be seen that the average effective stress decreased until the sheets were fully penetrated (zone 2). As the deformation continued, the stage of joint forming began. Specifically, the top sheet gradually and unevenly filled the ring grooves due to the nonuniform heat generated in the joint areas. The underside of the bottom sheet formed a draught wrapping the rivet shank. The average effective stress fluctuated up and down, but the overall trend was increasing (zone 3). When the riveting was finished, the residual stress of the joint was mainly concentrated in the metal sheets area, especially in HSS sheet. In addition, the ring grooves of the rivet head and nail shank were partially filled with the sheet material. The bottom sheet wrapped around the shank thus formed a mechanical interlocking structure (zone 4). To sum up, the deformation of the joint was due to the flow of sheets around the rivet. The deformed regions of sheets were concentrated near the rivet shank. However, local investigations of

average effective stress evolution inside the zone subjected to fracture revealed that the sheets underwent totally different stress-state in their fracture area: the stress increased, decreased, fluctuated, and finally reached the residual stress equilibrium state.

The Al/HSS E-HSN samples with different discharge energies are shown in Fig. 11. It could be found that the riveted specimens under the discharge energies of 5.1 kJ and 5.3 kJ had better wrapping behaviors of the HSS sheet to the nail shank. At the discharge energy of 4.9 kJ, the riveting was not completed. At the discharge energy of 5.5 kJ, the nail tip was severely crushed, and the HSS sheet was poorly wrapped on the rivet shank. The draught of the HSS sheet was bifurcated, resulting in loose joints and unsatisfactory riveted samples.

## 4.2 Cross-section observation

Figure 12 shows the cross-section geometry of joints with different discharge energies. It could be seen that rivets had no obvious deformation. The sheets were significantly

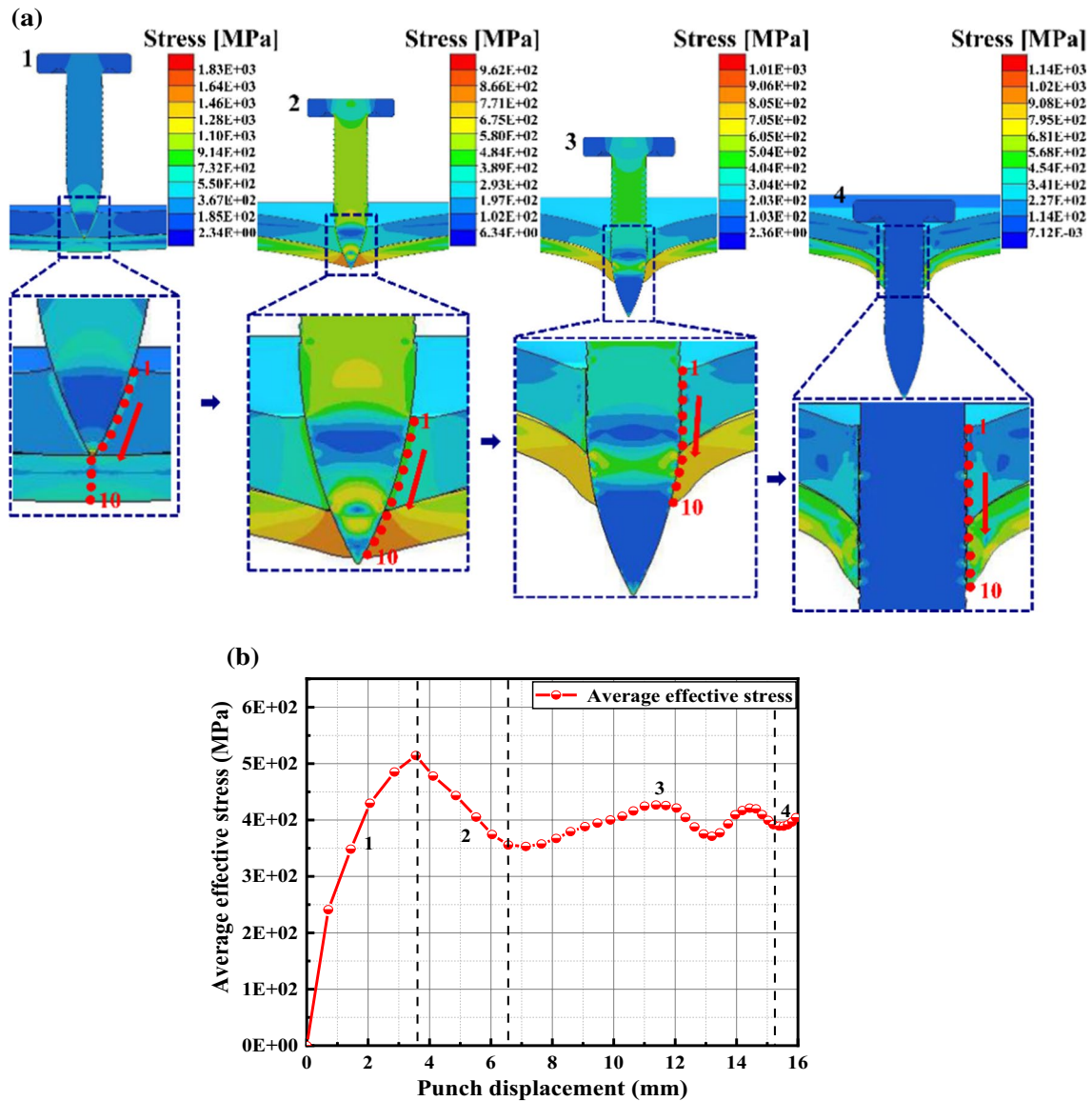
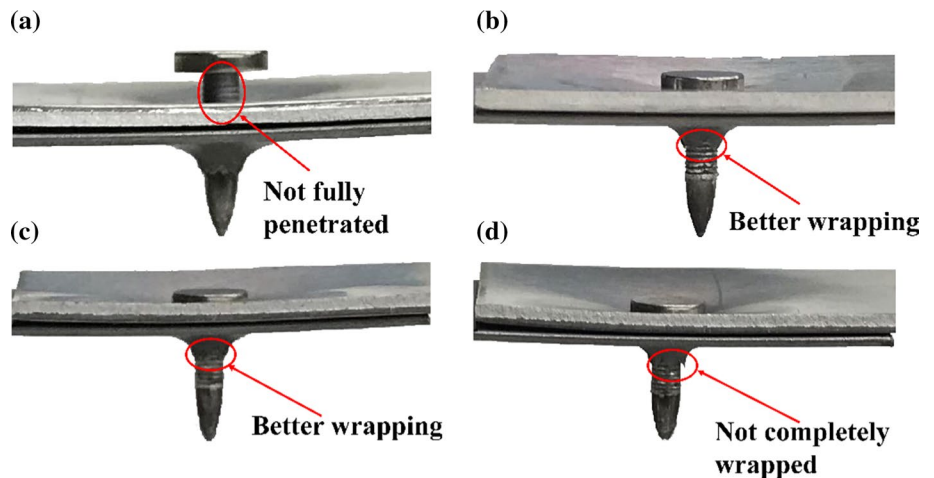
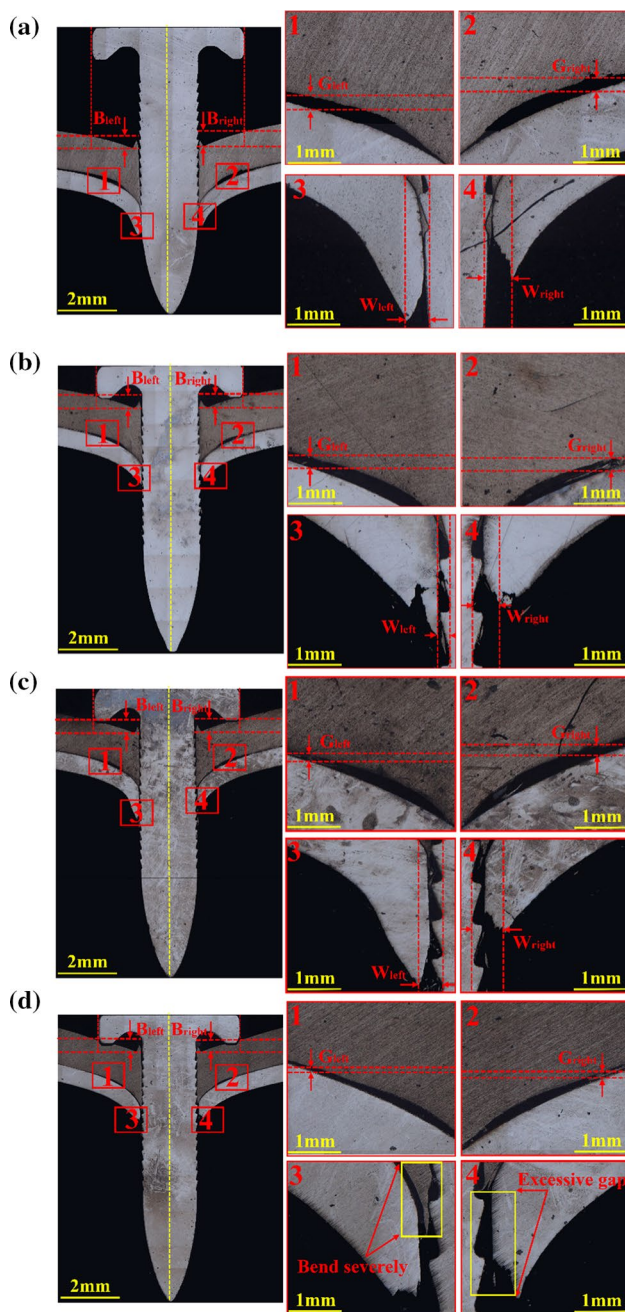


Fig. 10 The formation process of the joint: **a** the measured points located inside the sheets failure area, **b** average effective stress evolution

Fig. 11 The E-HSN specimens with different discharge energies: **a** 4.9 kJ, **b** 5.1 kJ, **c** 5.3 kJ, **d** 5.5 kJ







**Fig. 12** The cross-section geometries of the E-HSN joints with different discharge energies: **a** 4.9 kJ, **b** 5.1 kJ, **c** 5.3 kJ, **d** 5.5 kJ

deformed near the fracture area, and there was almost no deformation in other parts. This observation further indicated that highly localized deformation occurred only around the rivet penetration zone. In addition, for the high discharge energy (5.5 kJ), excessive magnetic pressures caused severe bending of the Al sheet. The HSS sheet was severely damaged and was not firmly connected to the rivet shank and Al sheet.

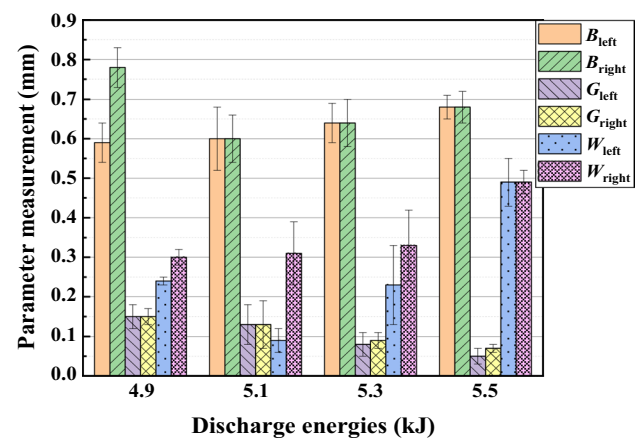
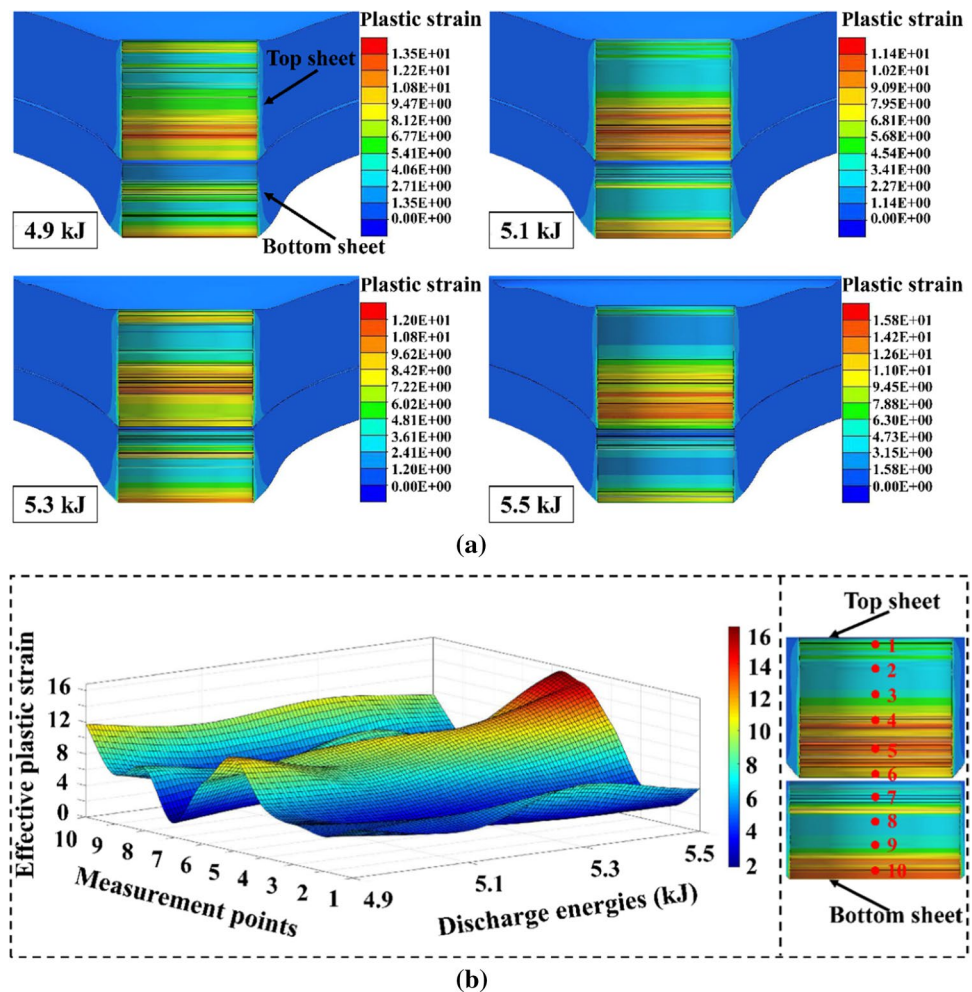


**Fig. 13** The measured parameters for the cross-section geometries of the E-HSN joints

The comparison of the three cross-sectional parameters for the joints was one of the most effective ways to evaluate the joints quality. Figure 13 shows measured parameters for the cross-section geometries of the joints. Three tests were repeated for each discharge energy and the average values of the structural parameters were measured. Firstly, it could be seen that most of the parameter values in the left and right parts showed relatively high consistency. Besides, the  $B$  values increased as the increase in the discharge energy, which meant the bending degree of the sheets gradually increased. Observing the  $G$  values, it could be found that the riveted joints showed good symmetry under different energy. The values gradually decreased as the discharge energy increased, which meant that the contact area between the sheets increased. As for the comparison of  $W$  values, it was not difficult to see that the high discharge energy (5.5 kJ) showed the maximum value. This meant that the draught of HSS sheet formed a poor wrapping to the rivet shank. With the continuous increase in the discharge energy, excessive deformation of the Al sheet caused serious damage to the HSS sheet, thereby making the joint more susceptible to failure. Therefore, the discharge energy of 5.1 kJ and 5.3 kJ were the suitable process parameters.

In order to better understand the variation trend of structural parameters under different discharge energy, the effective plastic strain of the sheet was analyzed. Figure 14a shows the effective plastic strain field in sheets obtained during numerical simulations of the sheets after riveting. It could be observed that the distribution of plastic deformation for sheets was different apparently. Figure 14b shows the strain distribution on the measured routes in the fracture area. For each route, 10 measured points were selected regularly. Obviously, the lower edge region of the sheets (Point 5, 6, 10) had a higher strain, which was prone to damage such as microcracks and breakage. For the Al sheet, the lower

**Fig. 14** Effective plastic strain in sheets obtained during numerical simulations of the sheets after riveting: **a** plastic strain field, **b** strain distribution in the fracture area



edge region (Point 5, 6) exhibited the largest plastic strain at the discharge energy of 5.5 kJ. The draught area of the HSS sheet (Point 10) was the smallest. The larger plastic deformation caused the Al sheet to seriously crush the HSS sheet, thereby preventing the Al sheet from forming a stable connection with the HSS sheet. In order to ensure that the HSS sheet still had a higher strength without cracking, the plastic deformation in the lower edge region of Al sheets should be prevented from being too large.

### 4.3 Shear properties

Three repeated shear tests were performed on samples at different discharge energies. The riveted joints at the discharge energy of 5.5 kJ loosened easily, which were not tested. Figure 15a shows typical shear load–displacement curves. The results of repeated experiments with the maximum shear load (MSL) are shown in Table 4. It could be observed that under the discharge energy of 5.1 kJ and 5.3 kJ, the shear load–displacement trend of the joints was similar. The MSL of joints under the discharge energy of 5.3 kJ was

higher than that of 5.1 kJ. However, the joint under the discharge energy of 5.1 kJ had the longest shear displacement. The shear failure processes of riveted joints are shown in Fig. 15b. Under three kinds of discharge energy, the shearing resistance process and failure mode of joints were basically the same. The Al sheets were bent and deformed, and no visible plastic deformation was observed in the rivets. Finally, the rivets were detached from the HSS sheets.

In the shear resistance process of riveted joints, the shear load–displacement curves could be divided into three stages. Under the pure shear load, the shear load increased gradually with the increase in displacement. Then the load gradually flattened and slowly increased until the maximum load was reached (Location 1). In this stage, the Al sheet began to bend and the rivet gradually inclined. The contact area between the rivet head and the Al sheet was continuously increasing. With the displacement continued to increase, the asymmetry load increased the bending angle of the Al sheet and the inclination of the rivet. Due to the decrease in the contact area between sheets, the friction decreased rapidly, and the shear load

**Fig. 15** The shear properties of the joints with different discharge energy: **a** the shear load–displacement curves, **b** the shear failure processes

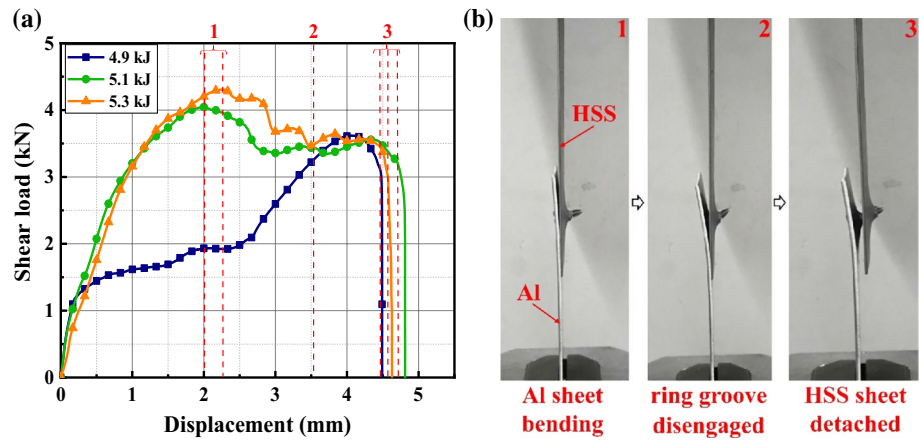


**Table 4** Maximum shear loads (MSL) for different discharge energy tests (kN)

Samples	MSL for 4.9 kJ	MSL for 5.1 kJ	MSL for 5.3 kJ
1	3.62	4.05	4.31
2	3.95	4.17	3.95
3	3.49	3.97	4.53
Average	3.69	4.06	4.26

was mainly provided by the interlocking force between the rivet shank and sheets. The ring grooves on one side of the rivet shank gradually disengaged from the sheets. Meanwhile, the nail shank began to twist because the sheets that filled with the ring grooves were gradually stripped (Location 2). After an approximate displacement of 4.5 mm, the rivet shank had been twisted enough to spread a crack at the shank-sheet junction and triggered global fracture. The detachment of the ring grooves on one side caused the HSS sheet to escape from the rivet. Some residual material remained attached to the rivet shank after failure (Location 3).

Figure 16 shows the shear failure appearance of lap joints.  $\theta$  represented the angle between the warping plane of the defining sheets and the vertical plane. Due to the combined action of clamps and rivets, the joint was subjected to a bending moment along the horizontal axis. Therefore, it caused different degrees of warpage at the shorter free end. It could be found that as the discharge energies increased, the value of  $\theta$  gradually increased. The energy absorption value of the joints was characterized by the warpage angle of the Al sheet. The energy absorption of the joint during shear process increased with the warpage angle. The tight degree of the connection between the rivet and Al sheet was higher than the wrapping structure formed by the rivet and HSS sheet. Therefore, the rotational deformation of the rivet caused by the warpage of the Al sheet destroyed the interlocking structure of the joints to some extent.

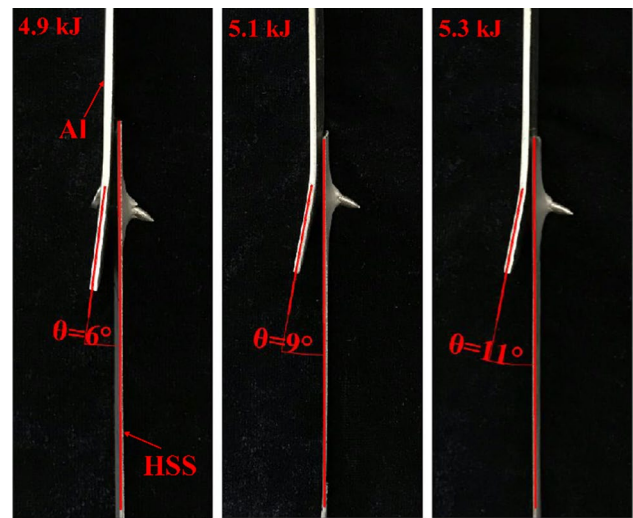


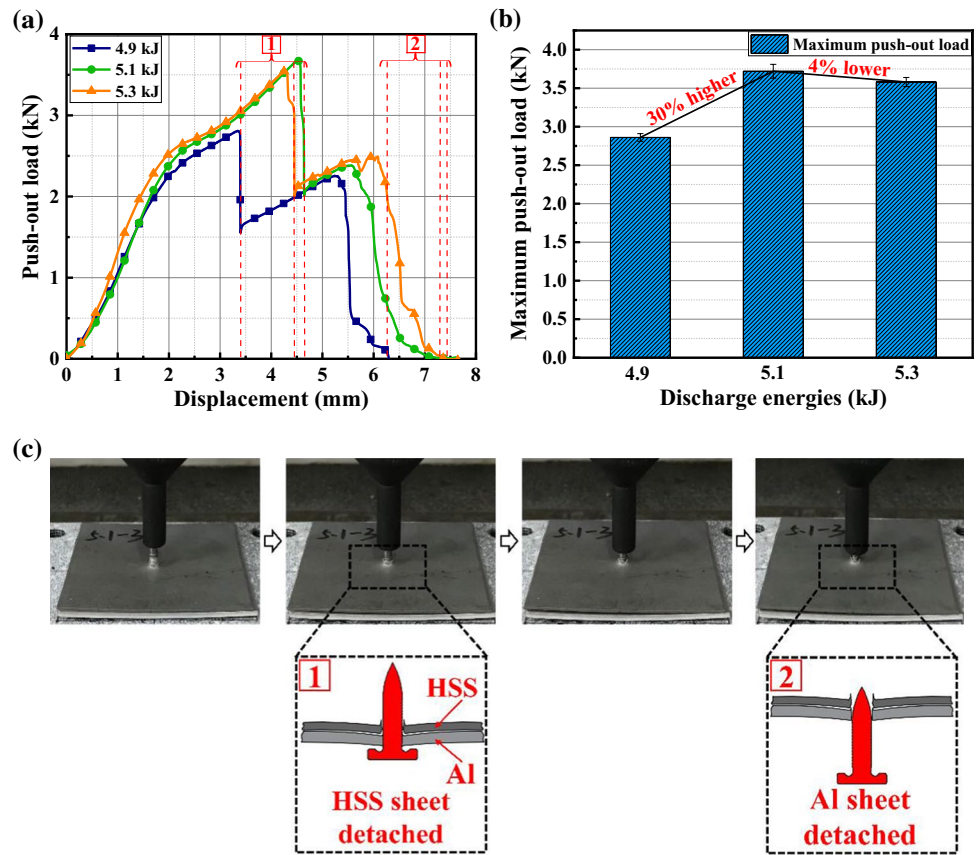
**Fig. 16** The shear failure appearance of the joints

### 4.4 Push-out properties

Typical push-out load–displacement curves are shown in Fig. 17a. It could be observed that the trends of curves were basically the same. The inflection points in the curves corresponded to the yield of sheets. Compared with the shear curves as shown in Fig. 15a, the push-out curves revealed a smaller peak load. In addition, it could be seen from Fig. 17b that the samples with the discharge energy of 5.1 kJ had the maximum push-out load (MPL). Figure 17c shows the push-out failure processes. When the punch pressed the rivet, the rivet moved down. The push resistance mainly provided by the friction between the sheet and grooves in the rivet.

Moreover, as shown in Fig. 17a, the push-out load–displacement curves exhibited roughly two cycle changes. The peak value of the first cycle was higher than the second one. Specifically, at the end of the first cycle, the rivet just detached from the HSS sheet, which meant that the riveted joints were failed (Location 1). As the punch continued to

**Fig. 17** The push-out properties of the joints: **a** the push-out load–displacement curves, **b** the maximum push-out load, **c** the failure processes



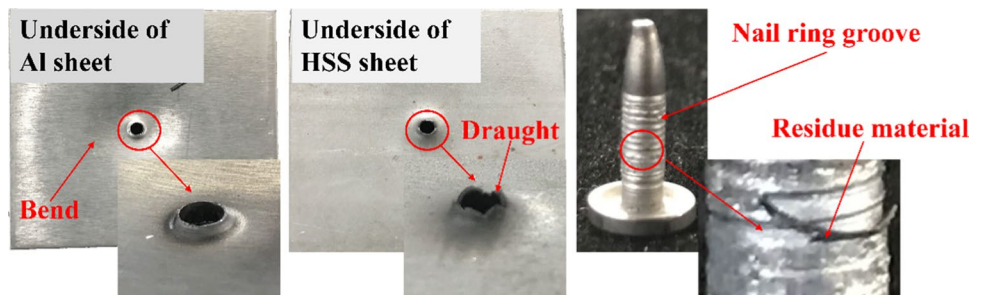
push down, the Al sheet eventually detached from the rivet shank (Location 2). The MPL value with discharge energy of 5.1 kJ was respectively 30% and 4% higher than that with discharge energy of 4.9 kJ and 5.3 kJ. It should be noted from Sect. 4.2 that at the discharge energy of 5.1 kJ, the distance  $W$  between the HSS sheet and the rivet shank was slightly shorter than that of other discharge energies. This indicated that the wrapping and interlocking degree of sheets was the best at the discharge energy of 5.1 kJ. Therefore, the riveted joints under the discharge energy of 5.1 kJ showed higher strength in the push-out tests.

Figure 18 shows the failure sheets and rivet after the push-out tests. It could be seen that the tip of the nail portion was crushed and deformed. The sheets around the rivet

experienced the bends. The Al sheet was more bent. After the failure, some residue material was also visible on the rivet shank due to the fracture of sheets filled with the ring grooves of the nail shank. Unlike the shear failure, the sheets that filled with the ring grooves of the nail shank as well as the draught portion of the HSS sheet were broken off.

In summary, presented investigation show that high-speed nailing process driven by electromagnetic force for dissimilar materials is feasible. Compared with conventional pneumatic drive, electromagnetic drive can stably provide a higher speed and larger impact load, which can more easily join the high strength steel sheet. Furthermore, the maintenance of discharging coil is convenient and the process is more environmentally friendly [18]. Therefore,

**Fig. 18** Deformed specimen after the push-out tests



with the development of automobile industry, it is of considerable significance to employ the E-HSN process in automotive assembly.

## 5 Conclusions

In this paper, a new E-HSN process was proposed. The connection mechanism analysis, mechanical properties and microtopography of 5052 Al/DP590 HSS E-HSN joints under different discharge energies were studied by numerical simulation and experiments. From the numerical analysis and experimental results, the following conclusions could be drawn:

1. The residual stress of the joint was mainly concentrated in the metal sheets area, especially in HSS sheet. Local investigations of average effective stress evolution inside the zone subjected to fracture revealed that the sheets underwent totally different stress-state in their fracture area: the stress increased, decreased, fluctuated and finally reached the residual stress equilibrium state.
2. The cross-section observations results showed that the riveted joints had good symmetry under all discharge energies. Besides, the draught of HSS sheet formed an excellent wrapping to the rivet shank at the discharge energy of 5.1 kJ and 5.3 kJ. It indicated that the joint was more firm under these two discharge parameters.
3. The samples with the discharge energy of 5.3 kJ had the highest maximum shear load, while the joints at the discharge energy of 5.1 kJ had the longest shear displacement. After an approximate displacement of 4.5 mm, the rivet shank had been twisted enough to spread a crack at the shank-sheet junction and triggered global fracture. The rivet stayed in the Al sheet eventually.
4. The samples with the discharge energy of 5.1 kJ had the maximum push-out load, which was due to the better wrapping and interlocking degree of the joints. All the joints failed in the destruction of the sheets that filled with the ring grooves of the nail shank as well as the draught portion of the HSS sheet.

**Acknowledgements** This project is supported by the National Natural Science Foundation of China (No. 51975202) and the Natural Science Foundation of Hunan Province (2019JJ30005), the National Key Research and Development Program of Hunan Province (2017GK2090).

**Data availability** The raw/processed data required to reproduce these findings cannot be shared at this time due to technical or time limitations.

## Compliance with ethical standards

**Conflict of interest** The authors declare that they have no conflict of interest.

## References

1. Lee MS, Seo HY, Kang CG. Comparative study on mechanical properties of CR340/CFRP composites through three point bending test by using theoretical and experimental methods. *Int J Precis Eng Manuf Green Technol.* 2016;3(4):359–65.
2. Sun X, Khaleel MA. Dynamic strength evaluations for self-piercing rivets and resistance spot welds joining similar and dissimilar metals. *Int J Impact Eng.* 2007;34(10):1668–82.
3. Laforte LP, Lebel LL. Thermal analysis and degradation of properties in carbon fiber/epoxy laminate riveting at high temperatures. *Polym Test.* 2018;67:205–12.
4. Groche P, Wohletz S, Brenneis M, Pabst C, Resch F. Joining by forming—a review on joint mechanisms, applications and future trends. *J Mater Process Technol.* 2014;214(10):1972–94.
5. Martinsen K, Hu SJ, Carlson BE. Joining of dissimilar materials. *CIRP Ann Manuf Technol.* 2015;64(2):679–99.
6. Chastel Y, Passemard L. Joining technologies for future automobile multi-material modules. *Procedia Eng.* 2014;81:2104–10.
7. Zhang HY. Influence of riveting sequence/direction on distortion of steel and aluminum sheets. *J Manuf Process.* 2020;53:304–9.
8. Chowdhury N, Chiu WK, Wang J, Chang P. Static and fatigue testing thin riveted, bonded and hybrid carbon fiber double lap joints used in aircraft structures. *Compos Struct.* 2015;121:315–23.
9. Skorupa M, Skorupa A, Machniewicz T, Korbel A. Effect of production variables on the fatigue behaviour of riveted lap joints. *Int J Fatigue.* 2010;32(7):996–1003.
10. Zhang X, Jiang H, Luo T, Hu L, Li GY, Cui JJ. Theoretical and experimental investigation on interference fit in electromagnetic riveting. *Int J Mech Sci.* 2019;156:261–71.
11. Repetto EA, Radovitzky R, Ortiz M, Lundquist RC, Sandstrom DR. A finite element study of electromagnetic riveting. *ASME J Manuf Sci Eng.* 1999;121(1):61–8.
12. Cui JJ, Qi L, Jiang H, Li GY, Zhang X. Numerical and experimental investigations in electromagnetic riveting with different rivet dies. *Int J Mater Form.* 2017;11(6):839–53.
13. Huffer BW. HH54 rugged and reliable handheld EMR. *SAE Int Aerosp Technol Conf Expo.* 2009. <https://doi.org/10.4271/2009-01-3267>.
14. Li GY, Jiang H, Zhang X, Cui JJ. Mechanical properties and fatigue behavior of electromagnetic riveted lap joints influenced by shear loading. *J Manuf Process.* 2017;26:226–39.
15. Liang JS, Jiang H, Zhang JS, Wu XH, Zhang X, Li GY, Cui JJ. Investigations on mechanical properties and microtopography of electromagnetic self-piercing riveted joints with carbon fiber reinforced plastics/aluminum alloy 5052. *Arch Civ Mech Eng.* 2019;19(1):240–50.
16. Sønstabø JK, Holmstrøm PH, Morin D, Langseth M. Macroscopic strength and failure properties of flow-drill screw connections. *J Mater Process Technol.* 2015;222:1–12.
17. Sønstabø JK, Morin D, Langseth M. Testing and modelling of flow-drill screw connections under quasi-static loadings. *J Mater Process Technol.* 2018;255:724–38.
18. Nagel P, Meschut G. Flow drill screwing of fibre-reinforced plastic-metal composites without a pilot hole. *Weld World.* 2017;61:1057–67.

19. Gao DL, Ersoy U, Stevenson R, Wang PC. A new one-sided joining process for aluminum alloys: friction stir blind riveting. *ASME J Manuf Sci Eng.* 2009;131(6):061002–11.
20. Meschut G, Hein D, Gerkens M. Numerical simulation of high-speed joining of sheet metal structures. *Procedia Manuf.* 2019;29:280–7.
21. Goldspiegel F, Mocellin K, Michel P. Numerical modelling of high-speed nailing process to join dissimilar materials: metal sheet formulation to simulate nail insertion stage. *J Mater Process Technol.* 2019;267:414–33.
22. Jiang H, Li GY, Zhang X, Cui JJ. Fatigue and failure mechanism in carbon fiber reinforced plastics/aluminum alloy single lap joint produced by electromagnetic riveting technique. *Compos Sci Technol.* 2017;152:1–10.
23. Goldspiegel F, Mocellin K, Michel P. Numerical simulation of high-speed nailing process. In: Presented at the 20th international ESAFORM conference on material forming (ESAFORM 2017), AIP conference proceedings 1896, Dublin, Ireland. 2017. <https://doi.org/10.1063/1.5008138>.
24. Jiang H, Luo T, Li GY, Zhang X, Cui JJ. Fatigue life assessment of electromagnetic riveted carbon fiber reinforce plastic/aluminum alloy lap joints using Weibull distribution. *Int J Fatigue.* 2017;105:180–9.
25. Carandente M, Dashwood RJ, Masters IG, Han L. Improvements in numerical simulation of the SPR process using a thermo-mechanical finite element analysis. *J Mater Process Technol.* 2016;236:148–61.
26. Johnson GR, Cook WH. A constitutive model and data for metals subjected to large strains, high strain rates and temperatures. In: *Proceedings of the 7th international symposium on ballistics.* The Hague; 1983. pp. 541–547.
27. Zener C, Hollomon H. Effect of strain-rate upon the plastic flow of steel. *J Appl Phys.* 1944;15(1):22–7.
28. Zheng YL, Chen WJ, Ren WD, Li JF, Zheng ZQ, Peng ZW. Flow stress behavior of 5052 aluminum alloy under hot compression deformation. *Alum Fabr.* 2007;2:17–20.
29. Qiu L, Tang JM, Liu HG. Constitutive relationship and hot processing pattern of high-strength steel DP590 based on hot tensile test. *Forg Stamp Technol.* 2017;42(1):121–5.

**Publisher's Note** Springer Nature remains neutral with regard to jurisdictional claims in published maps and institutional affiliations.